BMC Medical Imaging

RESEARCH Open Access

# Multiple deep learning models based on MRI images in discriminating glioblastoma from solitary brain metastases: a multicentre study

Chao Kong[1,2], Ding Yan[3], Kai Liu[4], Yong Yin[2,5*] and Changsheng Ma[2,5*]

## Abstract

**Objective** Development of a deep learning model for accurate preoperative identification of glioblastoma and solitary brain metastases by combining multi-centre and multi-sequence magnetic resonance images and comparison of the performance of different deep learning models.

**Methods** Clinical data and MR images of a total of 236 patients with pathologically confirmed glioblastoma and single brain metastases were retrospectively collected from January 2019 to May 2024 at Provincial Hospital of Shandong First Medical University, and the data were randomly divided into a training set and a test set according to the ratio of 8:2, in which the training set contained 197 cases and the test set contained 39 cases; the images were preprocessed and labeled with the tumor regions. The images were pre-processed and labeled with tumor regions, and different MRI sequences were input individually or in combination to train the deep learning model 3D ResNet-18, and the optimal sequence combinations were obtained by five-fold cross-validation enhancement of the data inputs and training of the deep learning models 3D Vision Transformer (3D Vit), 3D DenseNet, and 3D VGG; the working characteristic curves (ROCs) of subjects were plotted, and the area under the curve (AUC) was calculated. The area under the curve (AUC), accuracy, precision, recall and F1 score were used to evaluate the discriminative performance of the models. In addition, 48 patients with glioblastoma and single brain metastases from January 2020 to December 2022 were collected from the Affiliated Cancer Hospital of Shandong First Medical University as an external test set to compare the discriminative performance, robustness and generalization ability of the four deep learning models.

**Results** In the comparison of the discriminative effect of different MRI sequences, the three sequence combinations of T1-CE, T2, and T2-Flair gained discriminative effect, with the accuracy and AUC values of 0.8718 and 0.9305, respectively; after the four deep learning models were inputted into the aforementioned sequence combinations, the

*Correspondence:
Yong Yin
yinyongsd@126.com
Changsheng Ma
machangsheng_2000@126.com

Full list of author information is available at the end of the article

accuracy and AUC of the external validation of the 3D ResNet-18 model were 0.8125, respectively, 0.8899, all of which are the highest among all models.

**Conclusions** A combination of multi-sequence MR images and a deep learning model can efficiently identify glioblastoma and solitary brain metastases preoperatively, and the deep learning model 3D ResNet-18 has the highest efficacy in identifying the two types of tumours.

**Keywords** Deep learning, Glioblastoma, Solitary brain metastasis, Magnetic resonance imaging, Companion diagnostic system

## Introduction

As a common intracranial malignant tumor in adults, glioblastoma accounts for about 49% of primary malignant brain tumors, and this highly aggressive tumor not only has a high incidence rate, but also has a relatively poor clinical prognosis [1]. According to statistics, the average survival time of patients with glioblastoma is about 15 months, and the 5-year survival rate is only about 7% [2–3]; in contrast, brain metastases are the most common brain tumors in adults, and the incidence of brain metastases is higher compared with that of primary brain tumors, with about 20–40% of cancer patients experiencing brain metastases in the course of their disease [4–5]. The high incidence and diversity of brain metastases make them a major challenge for clinical diagnosis and treatment. Clinicians are able to correctly diagnose brain metastases in patients with a clear history and the presence of multiple foci; however, approximately 25–30% of brain metastases are usually single foci, and some brain metastases are diagnosed with neurologic symptoms on clinical examination [6, 7], resulting in misdiagnosis in approximately 40% of clinical cases [8, 9]; because the treatment options for glioblastomas and single brain metastases are not identical, it is important to Magnetic resonance examination for early identification of the two is the preferred noninvasive modality for neurological tumors [10], and different magnetic resonance imaging techniques can provide a wealth of information; however, glioblastomas and solitary brain metastases usually have similar imaging manifestations, such as cystic necrosis, ring enhancement, and peritumoral edema [11–12], and thus, identifying the two by the naked eye alone can be a great challenge.

In recent years, the joint application of imaging histology and MR images has achieved promising results in the field of tumor identification, and the computer model can automatically extract image information that is difficult to be found by the human eye and carry out autonomous learning, which, combined with different MR imaging techniques, provides a powerful tool for tumor identification [13], some studies [14] applied machine learning and MR images to construct glioblastoma and single brain metastases discriminative model, and achieved better results, but traditional machine learning needs to spend a lot of energy on the preprocessing of MR images, such as region of interest outlining, feature selection, etc. [15]; Deep learning, as an emerging technology, has gained wide attention in the field of image analysis in recent years. Compared with machine learning, it has stronger performance while saving data processing time [16]. Deep learning (DL), which relies on multi-layer neural network architecture and simulates the processing of the human brain, has demonstrated its powerful ability in several fields, and has gained wide attention as an emerging technology in the field of image analysis. Compared with machine learning, it has stronger image detection and analysis performance while saving data processing time [17]. First, its algorithm can intelligently and automatically carry out feature extraction, which greatly reduces the human intervention link, significantly shortens the data processing time, and improves the work efficiency [18]. Secondly, the deep learning model is able to better capture complex patterns and high-dimensional features in the image through the multi-layer neural network structure, and comprehensively analyze the image in terms of texture, morphology, signal intensity changes, etc., so as to improve the accuracy of classification and identification [19, 20]. A study based on convolutional neural network (CNN) [21] achieved remarkable results by training on MRI image data, which not only can automatically identify and classify tumor types, but also provide more comprehensive diagnostic information by combining with the corresponding clinical data.The main structures of CNN are convolutional layer, pooling layer, and fully connected layer. The convolutional layer extracts features through convolutional operations, the pooling layer samples to reduce the size of the feature map, and the fully connected layer is used for the final classification or regression task, which is outstanding in image processing [22]; the performance of deep learning models based on the CNN architecture is continuously improved after the increase and iteration of the convolutional layer and the pooling layer, which are represented by the ResNet (Residual Neural Network), the DenseNet (Dense Connected Convolutional Network); at the same time, CNNs can also provide more comprehensive diagnostic information combined with the corresponding clinical data. At the same time, the emergence of Vision

Transformer (Vit), a deep learning model with the core of Self-Attention Mechanism and feed-forward neural network, brings us a different framework from CNN, which consists of Encoder, and in the structural design, it abandons the localization of CNN. abandons the local convolution operation of CNN and adopts the global attention mechanism to process the global information of the image, which is fundamentally different from the local feature extraction approach of CNN [23]. In addition, deep learning can continuously improve the analysis and judgment ability through continuous learning and updating, so as to provide more accurate and personalized medical services in clinical practice.

Most of the previous studies have focused only on a single application of a deep learning model in tumor identification. However, as in the case of machine learning, when facing the same dataset, different deep models exhibit significantly different discriminative abilities due to the differences in their structures, algorithms, and learning styles. Therefore, under the current research trend, it is undoubtedly of vital significance to explore the most efficient and accurate model for identifying tumors, in order to substantially improve the accuracy of tumor identification and thus promote the improvement of clinical diagnosis and treatment; in this study, we comprehensively collect and systematically organize routine MRI sequence images from two hospitals, normalize the images and individually or reasonably combine them, and then select the most effective deep learning model. In this study, we comprehensively collected and systematically organized routine MRI sequences from two hospitals, normalized the images and combined them individually or in a reasonable way, and then used them to train a deep learning model to identify the best sequence combinations for discriminating glioblastoma and solitary brain metastasis, and then trained four deep learning models with different architectures to comprehensively compare and analyze the evaluation metrics of the validation set of multicenter, so as to find the model with optimal discriminating efficiency.

## Materials and methods

### Patient population

This retrospective study was approved by the hospital's ethics management committee, and the patient informed consent component was exempted due to the retrospective nature of the analysis and the use of anonymized medical records (SDTHEC 2024001002). We included a total of 236 patients with glioblastoma ($n = 119$) and solitary brain metastases ($n = 117$) who underwent pretreatment MR examination at the Provincial Hospital of Shandong First Medical University between January 2019 and January 2024, of which 197 (GBM = 99, SBM = 98) served as the training set and 39 (GBM = 20, SBM = 19) as the internal validation set. Forty-eight patients (GBM = 20; SBM = 28) from the Affiliated Tumor Hospital of the First Medical University of Shandong Province served as the external validation set.

Inclusion Criteria: 1). Patients with a clear clinical diagnosis and pathological findings; 2) The patient's T1WI, T2WI, T1CE, and T2Flair images were complete; 3). The diameter of the tumor entity is ≥ 1.0 cm.

Exclusion criteria: 1). Patient had multiple brain tumors.2). Patient had any treatment before the MRI examination.3). Artifacts or noise in the patient's MR image.

The diagnosis of brain metastases in all patients was made by senior radiologists based on corresponding imaging data and clinical symptoms. All of the above information was obtained with the informed consent of the patient. The flow chart for patient enrolment is shown in Fig. 1.

### Image acquisition

During this study period, multiple MR devices used in both hospitals were from different vendors and had different scanning parameters. Five 3.0T MR machines and two 1.5T MR machines from the two hospitals were used for imaging with an 8-channel sensitivity-coded head coil, and the enhancement scans were performed in axial, sagittal, and coronal positions with T1WI scans, and the contrast agent used was gadopentetate dextran (Gd-DTPA), which was injected into the elbow vein at a flow rate of 3.0 mL/s at a rate of 0.1 mmoL/kg.MR images were acquired on a SYNGO. VIA system (Siemens Medical Systems) and acquired on a PACS (Picture archiving and communication system) workstation (Table 1).

### Image analysis and processing

In this study, images of four conventional MRI sequences, i.e., T1WI, T2WI, T2-FLAIR, and T1-CE, were selected to be input into the deep learning model; the screening of image quality was performed by two experienced radiologists, one with 3 years of diagnostic work experience in head and neck imaging, and the other with 10 years of relevant experience.The patients with GBM and SBM were screened according to the World Health Organization (WHO) classification criteria for central nervous system tumors in 2021. World Health Organization (WHO) classification criteria for CNS tumors were used for screening, and we defined the high signal region around the tumor entity in the T2-FLAIR sequence as the peri-tumor region and included it in the differential range, and applied it to the other three sequences according to this range.

This study is a multicenter experiment, and due to the differences in image acquisition methods and equipment in different hospitals, the gray-scale information of the

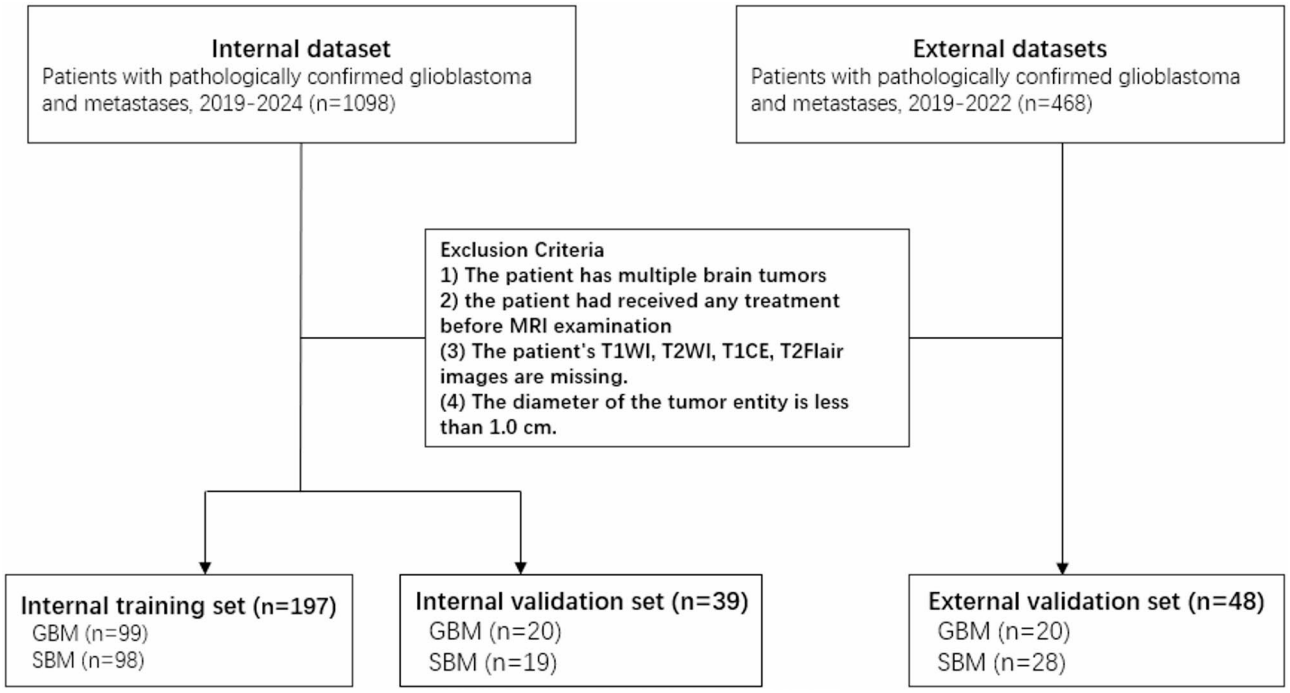


**Fig. 1** Patient enrolment flowchart

**Table 1** Different MR machines and scanning parameters

| Machines/ Parameters | Philips-Achieva | Philips- Ingenia CX | Siemens-Prisma | GE- Signa HD | GE MR750 | Siemens Amira | Siemens Avanto |
|---|---|---|---|---|---|---|---|
| **Strength(T)** | 3.0 | 3.0 | 3.0 | 3.0 | 3.0 | 1.5 | 1.5 |
| **T1WI** | | | | | | | |
| TR(ms) | 500 | 510 | 500 | 550 | 520 | 515 | 600 |
| TE(ms) | 15 | 12 | 16 | 11 | 12 | 10 | 9 |
| Slice(mm) | 5 | 5 | 5 | 5 | 5 | 5 | 5 |
| Gap(mm) | 6 | 6 | 6 | 6 | 6 | 6 | 6 |
| FOV(mm) | 240×289 | 200×241 | 230×230 | 260×260 | 240×240 | 230×277 | 220×220 |
| **T2WI** | | | | | | | |
| TR(ms) | 4000 | 3326 | 2139 | 2200 | 4975 | 5900 | 5000 |
| TE(ms) | 100 | 122 | 90 | 96 | 110 | 100 | 150 |
| Slice(mm) | 5 | 5 | 5 | 5 | 5 | 5 | 5 |
| Gap(mm) | 6 | 6 | 6 | 6 | 6 | 6 | 6 |
| FOV(mm) | 240×289 | 200×241 | 230×230 | 260×260 | 240×240 | 230×277 | 220×220 |
| **T2-FLAIR** | | | | | | | |
| TR(ms) | 9000 | 9000 | 7000 | 9000 | 8000 | 6000 | 9000 |
| TE(ms) | 2500 | 2600 | 125 | 2688 | 2386 | 2000 | 140 |
| Slice(mm) | 5 | 5 | 5 | 5 | 5 | 5 | 5 |
| Gap(mm) | 6 | 6 | 6 | 6 | 6 | 6 | 6 |
| FOV(mm) | 240×289 | 200×241 | 230×230 | 260×260 | 240×240 | 230×277 | 220×220 |
| **T1-CE** | | | | | | | |
| TR(ms) | 440 | 410 | 178 | 450 | 440 | 620 | 490 |
| TE(ms) | 10 | 9 | 5 | 15 | 10 | 15 | 12 |
| Slice(mm) | 5 | 5 | 5 | 5 | 5 | 5 | 5 |
| Gap(mm) | 6 | 6 | 6 | 6 | 6 | 6 | 6 |
| FOV(mm) | 240×289 | 200×241 | 230×230 | 260×260 | 240×240 | 230×277 | 220×220 |

same tissue may be biased on images acquired in different hospitals. In order to eliminate or reduce the errors caused by differences in image size and intensity, the images need to be normalized; the images of each patient were preprocessed using SimpleITK (an open-source image processing software based on python 3.7.0, https://github.com/SimpleITK/SimpleITK), and the images were resampled The images were resampled to $1 \times 1 \times 1$ $mm^3$ isotropic voxels, WhiteStripe normalization was used to equalize the overall intensity distribution of the images, and N4 bias-corrected intensity normalization was used to eliminate the bias field effect in the images due to the uneven magnetic field and other factors. Thereafter, two experienced radiologists manually drew rectangular ROIs on T1WI, T2WI, T2-FLAIR, and T1-CE images by 3D-Slicer (https://www.slicer.org) software, and a u niform standard was established before image outlining and segmentation, which was completed under the guidance of a senior imaging expert when differences were encountered. Compared with the fine outlining method of tumor entities in previous experiments, this study adopts a rectangular segmentation framework, which can more comprehensively show the tumor entities and peritumor high-signal areas while reducing the physician's image segmentation time, providing comprehensive information for the deep learning model, and improving the model's adaptive ability.

#### Deep learning model selection

In order to explore the performance of different models in medical image analysis tasks, this study introduces three classical CNN models, 3D ResNet-18, 3D DenseNet, 3D VGG, and 3D Vision Transformer (3D Vit) based on the Transformer architecture. 3D ResNet-18 convolutional layer consists of $7 \times 7 \times 7$ convolution and 64 filters, while 3D DenseNet consists of densely connected blocks. The 3D ResNet −18 convolutional layers are composed of $7 \times 7 \times 7$ convolutions and 64 filters, which effectively solves the gradient vanishing problem through residual connections; 3D DenseNet is composed of densely connected blocks, and its internal convolutional layers are set up in a way that helps to enhance the feature transfer and improve the model learning ability. 3D VGG consists of multiple $3 \times 3 \times 3$ convolutional layers stacked together, and each convolutional layer is operated immediately after using the Rectified Linear Unit (ReLU), which is the most powerful and efficient CNN model in the world. The 3D VGG consists of multiple $3 \times 3 \times 3$ convolutional layers stacked on top of each other, and each convolutional operation is immediately followed by a Rectified Linear Unit (ReLU) activation function, which introduces a nonlinear element to the neural network, allowing the model to learn more complex features and patterns in the data. 3D Vit is mainly composed of three parts: Patch Embedding, Transformer Encoder, and Multi-Layer Perceptron (MLP), and Patch Embedding partitions the image into multiple The patch embedding divides the image into multiple chunks and transforms them into feature vectors; the Transformer encoder models these feature vectors globally using the self-attention mechanism; and the MLP performs the final classification or regression task based on the features output from the encoder.

During the training process, the Adam optimizer is used, which is able to adaptively adjust the learning rate and performs well when dealing with large-scale datasets and complex models; the weight decay is set to 0.01, the batch size to 32, and the initial learning rate to 0.0001. Two measures are taken to prevent model overfitting: first, the loss function is added with an L2 penalty term for the weight, i.e., L2 regularization (L2 - Ridge), which limits the model complexity; second, the model is enhanced by a data enhancement method, i.e., random rotation (rotation by 90°), which enhances the model adaptation to images with different morphologies. Ridge) as a way to limit the model complexity; and secondly, through data enhancement methods, i.e., random rotation (rotating at 90°), thus enhancing the model's adaptability to different morphological images. In addition, we use a five-fold cross-validation method to obtain a comprehensive evaluation index of the model performance by averaging the results of five validations.

This study is based on Python version 3.7.0 and uses the PyTorch framework to train the above model on an NVIDIA GeForce RTX 3090 Ti graphics processor for up to 200 iterations. The performance of each model in the identification task is evaluated through the metrics of accuracy, recall, F1 value, and the area under the curve (AUC) of the subjects' work characteristics.

#### Deep learning model construction and evaluation

Among the total 236 patients in the internal dataset, 197 samples of GBM and SBM patients were included in the training group to construct the model according to the ratio of approximately 8: 2. 80% of the ratio can provide relatively sufficient samples for the model to be trained, so as to better fit the data, enable the model parameters to be efficiently updated and converged, and avoid overfitting; the other 39 samples were also included in the test group by random stratified sampling, and approximately 20% could provide enough data to accurately assess the generalization ability of the model on unknown data, so that the model could be optimized and adjusted; firstly, the single-sequence MRI model was constructed using images of four MRI sequences (T1WI, T2WI, T2-FLAIR, and T1-CE), and the area under the working characteristics (AUC), accuracy (ACC) of the subjects were also used, At the same time, the area under the working

characteristic (AUC), accuracy (ACC), precision (Precision), recall (Recall), F1 score and other indexes are used to comprehensively evaluate the classification performance of the single-sequence model; in order to improve the classification performance, the MR sequences with the optimal indexes are screened out from the above single-sequence model evaluation results, and then a combined model is constructed, which outputs for the classification of GBM and SBM, and compares the discriminative efficiencies of the combined model and the single-sequence model. This process is carried out based on 3D ResNet-18, which is due to the unique residual structure of the ResNet model that enables the model to efficiently extract multilevel features while maintaining parameter efficiency and training stability, especially for tumor identification tasks. At the same time, this study wishes to explore the possibility of new model architecture, so the self-attention mechanism model 3D Vit is introduced; after obtaining the optimal sequence combination we train the four deep learning models 3D ResNet-18, 3D DenseNet, 3D VGG, and 3D Vit at the same time. After the training is completed, the ROC curve is plotted, and the classification performance is evaluated by combining the AUC and ACC of the internal test set and the external validation set, thus comparing the differential diagnosis ability of the four models. The overall workflow diagram is shown in Fig. 2.

### Statistical analysis

CNN and Transformer model training was implemented using the PyTorch software package, and the five-fold cross-validation method was used to ensure the stability and generalization ability of the models. Data were statistically analyzed by SPSS 22.0 software: continuous variables (age) were tested for normality using the Kolmogorov-Smirnov test, independent samples t-tests were used to compare the differences between the GBM and SBM groups for those who conformed to a normal distribution, and the Mann-Whitney U test was used for those who did not have a normal distribution; and the chi-square test was used for the categorical variables (gender, tumor region). The scikit-learn software package was used to evaluate the discriminative efficacy of the deep learning model by obtaining the subject's work characteristic curve (ROC) and calculating the area under the curve (AUC), which was combined with the accuracy, precision, recall, and F1 score of the model's output to make a comprehensive judgment.

## Results

### Patient clinical characteristics

In this study, the internal dataset was divided into a training set and a test set based on a ratio of approximately 8: 2. The internal training set consisted of 197 patients (103 males and 94 females; mean age of GBM 58.9 (14) years, mean age of SBM 62 (12) years), and the internal test set consisted of 39 patients (21 males and 18 females; mean age of GBM 58 ± 13.3 years, mean age of SBM 63 ± 8.8 years). To assess the generalizability and robustness of the model, we nabbed 48 patients (29 males and 19 females; mean age of GBM 53 ± 13.1 years, mean age of SBM 58 ± 7.3 years) from another hospital as the external validation set. No statistical differences in age, gender, and tumor imaging characteristics were observed between GBM and SBM patients in the internal and

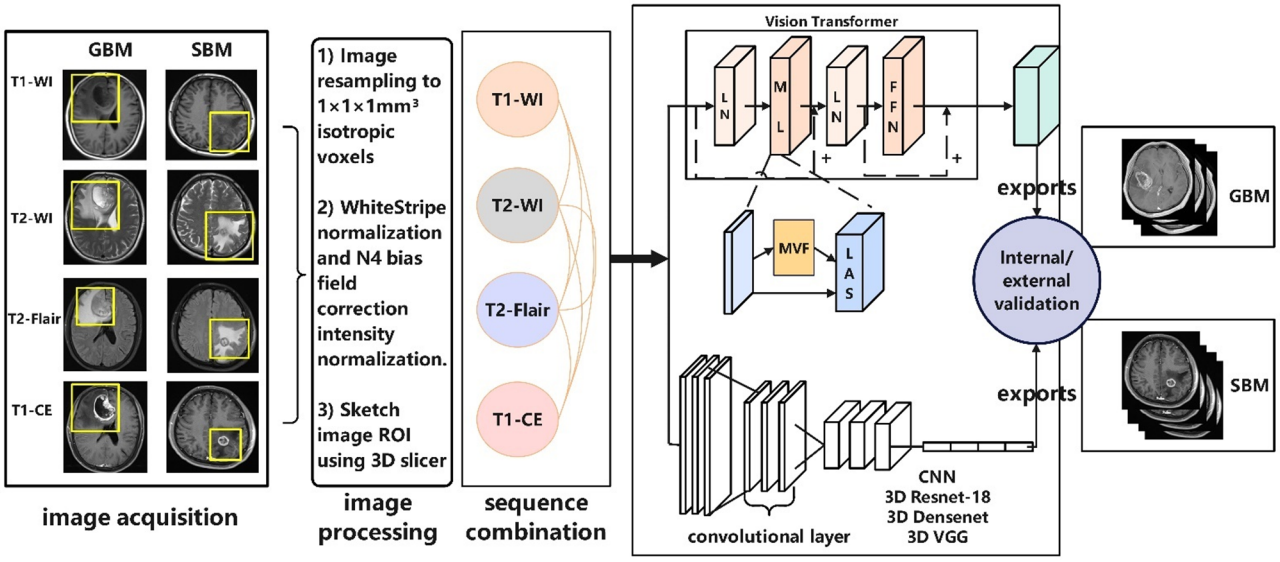


**Fig. 2** Workflow diagram. Note: LN: Layer Normalization: Mean Long Self-Attention Layer. MVF: Mean Value Filter. LAS: Long Attention Layer FFN: Feed-forward Neural Network. 3D ResNet-18, 3D DenseNet, 3D VGG are all based on the CNN network structure, and the schematic diagrams are shown in Fig

**Table 2** Clinical and demographic characteristics of patients

| | Training set | | *P* | Internal validation set | | *P* | External Validation Set | | *P* |
|---|---|---|---|---|---|---|---|---|---|
| | GBM | SBM | | GBM | SBM | | GBM | SBM | |
| **Quantities** | 99 | 98 | | 20 | 19 | | 20 | 28 | |
| **Age* (years)** | 58.9(14) | 62(12) | 0.053[a] | 58 ± 13.3 | 63 ± 8.8 | 0.08[b] | 52.6 ± 13.1 | 57.8 ± 7.4 | 0.181[b] |
| **Sex**[c] | | | | | | | | | |
| Male | 50 | 53 | >0.05 | 11 | 10 | >0.05 | 12 | 17 | >0.05 |
| Female | 49 | 45 | | 9 | 9 | | 8 | 11 | |
| **Location**[c] | | | | | | | | | |
| Supratentorial | 78 | 75 | >0.05 | 20 | 16 | >0.05 | 19 | 25 | >0.05 |
| Infratentorial | 21 | 23 | | 0 | 3 | | 1 | 3 | |
| **Hemorrhage**[c] | | | | | | | | | |
| Yes | 15 | 12 | >0.05 | 2 | 4 | >0.05 | 6 | 5 | >0.05 |
| No | 84 | 86 | | 18 | 15 | | 14 | 23 | |
| **Frontier**[c] | | | | | | | | | |
| Clearer | 17 | 20 | >0.05 | 6 | 3 | >0.05 | 4 | 8 | >0.05 |
| Blurred | 82 | 78 | | 14 | 16 | | 16 | 20 | |
| **Peritumoral edema**[c] | | | | | | | | | |
| Yes | 96 | 96 | >0.05 | 19 | 15 | >0.05 | 19 | 27 | >0.05 |
| No | 3 | 2 | | 1 | 4 | | 1 | 3 | |
| **Cranial Symptoms**[c] | | | | | | | | | |
| Yes | 99 | 95 | >0.05 | 19 | 14 | >0.05 | 20 | 25 | >0.05 |
| No | 0 | 3 | | 1 | 5 | | 0 | 3 | |

Note: *Normally distributed data are expressed as mean ± standard deviation, and non-normally distributed data are expressed as median (interquartile spacing); (a) Mann-Whitney U test; (b) independent samples T test; (c) chi-square test. $p > 0.05$ indicates that the difference is not statistically significant

**Table 3** Training results based on 3D ResNet-18 model for different MRI sequence internal datasets

| | Training set | | | | | Internal validation | | | | |
|---|---|---|---|---|---|---|---|---|---|---|
| | ACC | Precision | Recall | F1-score | AUC | ACC | Precision | Recall | F1-score | AUC |
| T2WI | 0.7975 | 0.7778 | 0.8182 | 0.7975 | 0.8910 | 0.7949 | 0.8182 | 0.8182 | 0.8182 | 0.8610 |
| T2-FLAIR | 1.0000 | 1.0000 | 1.0000 | 1.0000 | 1.0000 | 0.8205 | 0.7778 | 0.9545 | 0.8571 | 0.8663 |
| T1-CE | 1.0000 | 1.0000 | 1.0000 | 1.0000 | 1.0000 | 0.8205 | 0.8000 | 0.9091 | 0.8511 | 0.8690 |
| T1WI | 0.7179 | 0.8667 | 0.5909 | 0.7027 | 0.8262 | 0.7215 | 0.7797 | 0.5974 | 0.6765 | 0.8063 |
| T1CE + T2-FLAIR | 1.0000 | 1.0000 | 1.0000 | 1.0000 | 1.0000 | 0.8462 | 0.8077 | 0.9545 | 0.8750 | 0.9011 |
| T2WI + T1CE + T2-FLAIR | 0.9873 | 0.9747 | 1.0000 | 0.9872 | 0.9989 | 0.8718 | **0.8148** | **1.0000** | **0.8980** | **0.9305** |

external datasets. Table 2 shows the clinical baseline characteristics of all patients.(Table 2).

### Training results on internal datasets with different MR sequences

#### *Single MR sequence*

In the internal dataset, we first trained the 3D ResNet-18 model with four sequences, T1WI, T2WI, T2-FLAIR, and T1-CE, respectively, and after the training was completed, we compared the differential diagnosis performance of each model in the internal test set. The AUC, ACC, precision, recall, and F1 score of the deep learning model constructed based on the T1-CE sequence are 0.8690, 0.8205, 0.8000, 0.9091, and 0.8511 in the internal validation set in that order, and the values of the AUC and ACC are at the highest level among the single-sequence deep learning models; whereas the AUC, ACC, and F1 score of the T1WI sequence-based deep learning model based on T1WI sequences, its AUC, ACC, precision, recall, and F1 score in the internal validation set are 0.8063, 0.7215, 0.7797, 0.5974, 0.6765, respectively, and all the indexes are at the lowest level in the single-sequence deep learning model, in which the level of recall is lower than 0.6, which indicates that the model's recognition of the target category is not good, and it results in a misjudgement in the process of identification. The probability of misjudgment in the identification process is larger. The results of the deep learning model with a single MR sequence are shown in Table 3.

### MR sequential portfolio modelling

A Given the relatively low efficacy of T1WI in single-sequence deep learning models, in order to avoid potential bias and reduce model complexity, we exclude T1WI in multi-sequence combinations, and instead incorporate the relatively high single-sequence efficacy of the T1-CE and T2-FLAIR sequences to construct a two-channel model, which achieves an accuracy and an AUC of 0.8462,

**Table 4** Internal validation results for four deep learning models

| Model | ACC | Precision | Recall | F1-score | AUC |
|---|---|---|---|---|---|
| 3D ResNet-18 | **0.8718** | 0.8148 | **1.0000** | **0.8980** | **0.9305** |
| 3D Vit | 0.6154 | 0.5946 | 1.0000 | 0.7458 | 0.6765 |
| 3D DenseNet | 0.8462 | **0.8636** | 0.8636 | 0.8636 | 0.8690 |
| 3D VGG | 0.7179 | 0.7895 | 0.6818 | 0.7317 | 0.7059 |

0.9011, and 0.9011, respectively, in the internal validation set., all of which were superior to the single-sequence model. Considering that T2WI has a unique advantage in reflecting the water content of tissues, etc., and the previous study found that it has some value in the display of tumor-related features, to further improve the model performance, we introduced T2WI to construct a three-channel model based on T2WI, T1CE, and T2-FLAIR, whose accuracy and AUC were increased to 0.8718 and 0.9305, respectively, and recall was increased to 1.0000, which was better than the single-sequence model in the internal validation set. The accuracy and AUC were increased to 0.8718 and 0.9305, and the recall rate was increased to 1.0000, and the discriminative efficacy and tumor identification ability were significantly better than that of single-sequence and T1-CE + T2-FLAIR combination models. The results showed that multiple sequence fusion could synergistically enhance the tumor identification performance of the model (Table 3).

### Internal validation results of different deep learning models

The results of the internal validation sets for the four deep learning models are detailed in Table 4. We carried out training and internal validation of 3D DenseNet, 3D VGG, 3D VIT, and 3D ResNet-18 models using a combination of T2WI, T1CE, and T2-FLAIR images, respectively. In the internal validation set, the AUC, ACC, precision, recall, and F1 score of the 3D ResNet-18 model were 0.9305, 0.8718, 0.8148, 1.0000, and 0.8980, respectively, which gave the best results among the four models (Figs. 3 and 4).

### External validation results of different deep learning models

The results of the external validation sets of the four deep learning models are detailed in Table 5.The T2WI + T1-CE + T2-FLAIR sequence images from the external validation sets are inputted into the trained 3D ResNet-18, 3D DenseNet, 3D VGG, and 3D Vit, respectively. The AUC, accuracy, precision, recall, and F1 scores for the 3D ResNet-18 model are 0.8899, 0.8125, 0.7742, 0.9231, and 0.8421, respectively; the AUC, accuracy, precision, recall, and F1 score for the 3D ResNet-18 model are 0.8899, 0.8125, 0.7742, 0.9231, and 0.8421, respectively; collectively, the 3D ResNet-18 model has the best stability in each index (Figs. 5 and 6).

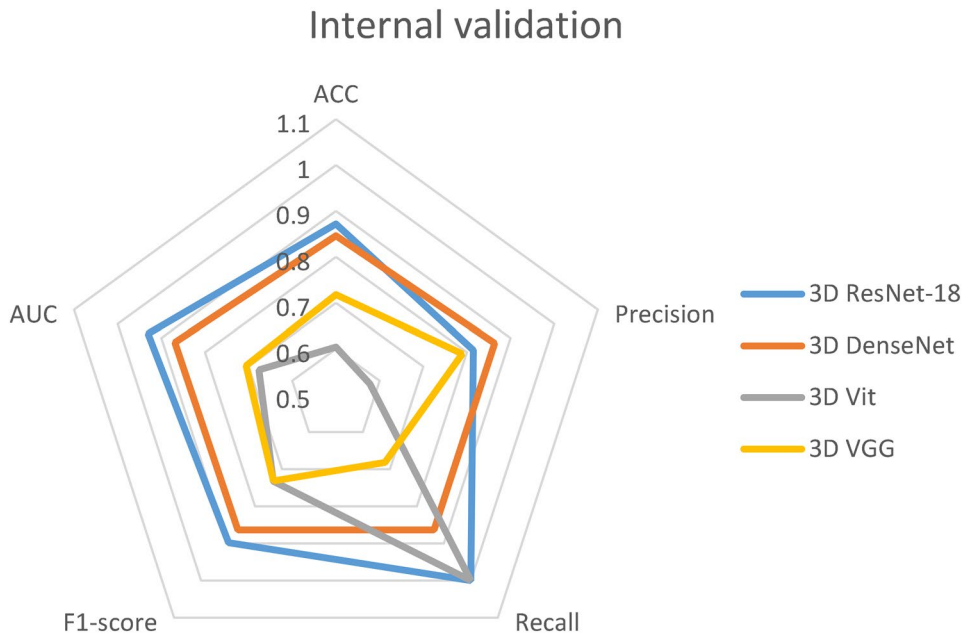


**Fig. 3** Radar chart of results from the internal test set of four deep learning models. Note: In the internal test set, 3D ResNet-18 performs well and balanced compared to the other three models in all evaluation metrics. This advantage stems from its residual linkage structure that effectively mitigates the gradient vanishing problem, the 3D convolutional layer's ability to capture voxel-level spatial features, and the parameter efficiency advantage (the number of parameters is only 42% of that of 3D ViT), which ensures the stability of the training and at the same time realizes the optimal balance between feature extraction and classification performance

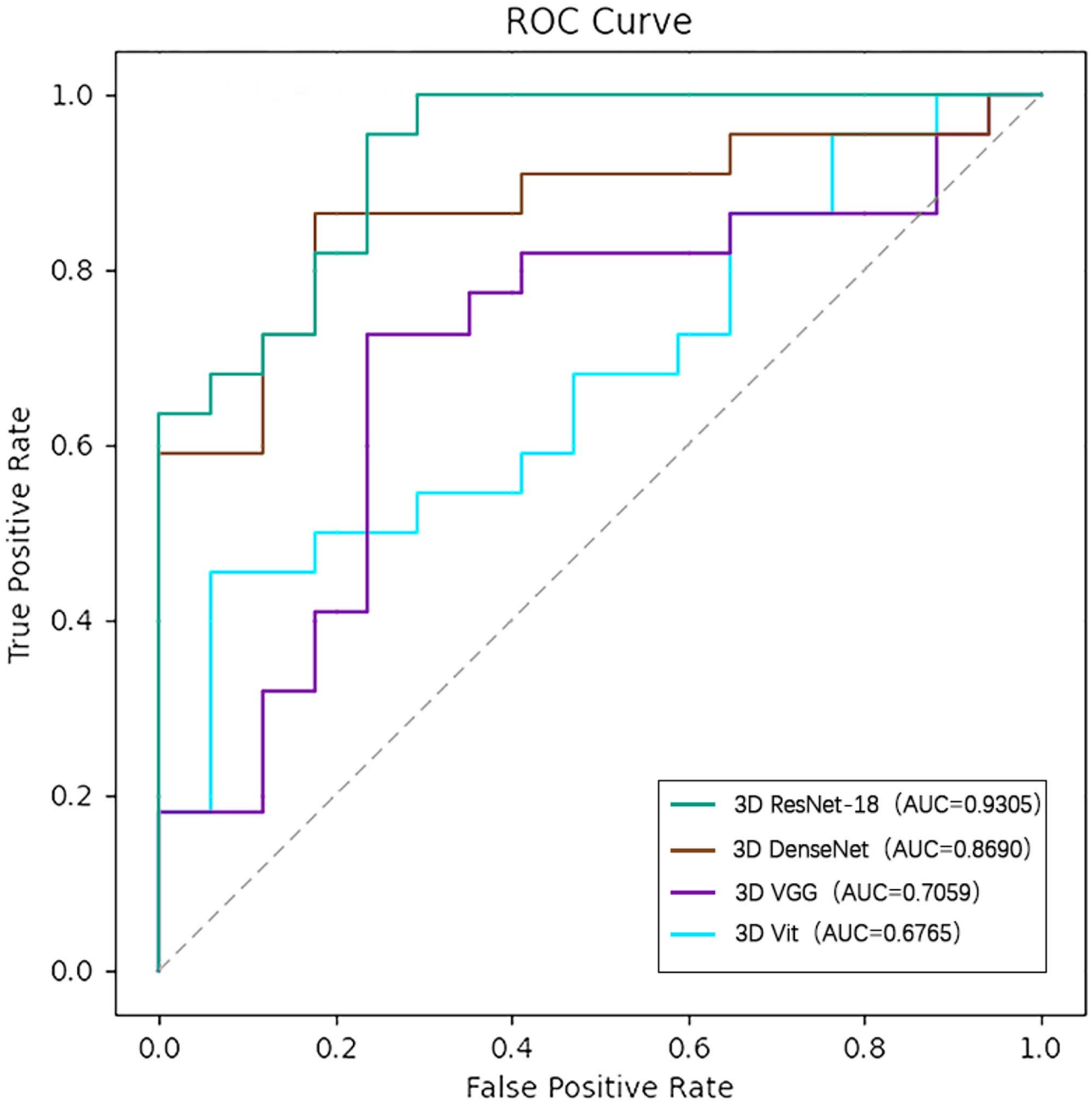


**Fig. 4** Internal validation of ROC curves for different deep learning models

**Table 5** External validation results for four deep learning models

| Model | ACC | Precision | Recall | F1-score | AUC |
|---|---|---|---|---|---|
| **3D ResNet-18** | **0.8125** | **0.7742** | 0.9231 | **0.8421** | **0.8899** |
| **3D Vit** | 0.6042 | 0.5778 | **1.0000** | 0.7324 | 0.6294 |
| **3D DenseNet** | 0.7708 | 0.7586 | 0.8462 | 0.8000 | 0.8287 |
| **3D VGG** | 0.6667 | 0.7083 | 0.6538 | 0.6800 | 0.7203 |

## Discussion

The differentiation between glioblastoma (GBM) and solitary brain metastasis (SBM) has always been a focus of attention for clinicians. Glioblastoma, as the most malignant glioma, is widely infiltrated within the brain tissue, progresses rapidly, and is highly prone to recurrence, and the tumor cells can undergo seeding through the cerebrospinal fluid circulation and be planted in other intracranial sites such as the ventricular system and the subarachnoid space [24]; SBM's There is no uniform data on the exact incidence of SBM, but the incidence of brain metastases has been reported to be up to nearly 30% in cancer patients [25], and in the face of patients initially diagnosed with intracranial symptoms, the similarity between the imaging manifestations of GBM and SBM

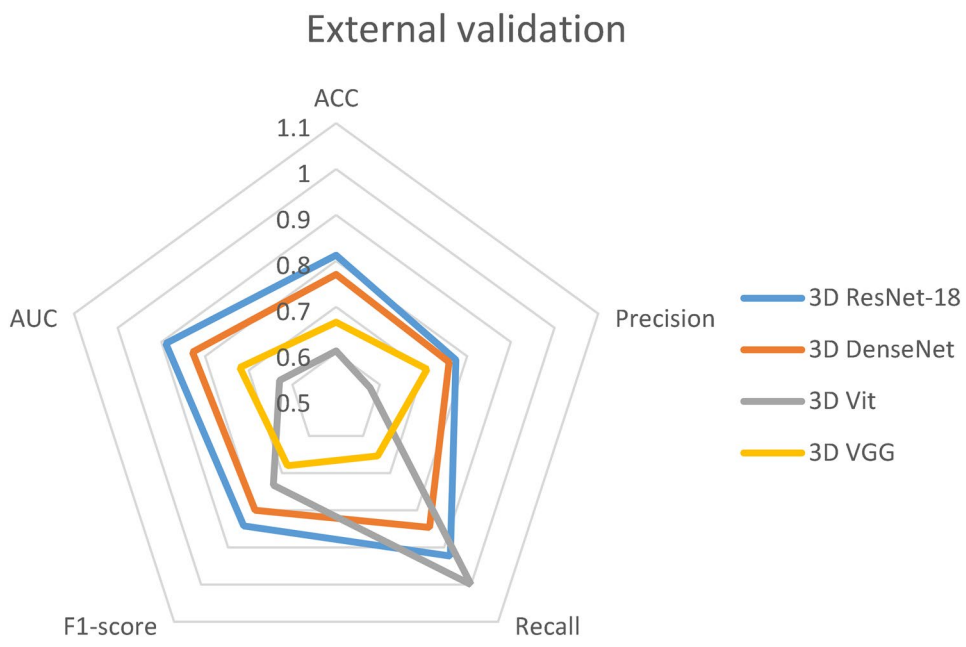


**Fig. 5** Radar chart of external validation results for four deep learning models. Note: 3D ResNet-18 has a balanced performance in all evaluation indexes, and its stability and accuracy are better than other models; 3D Vit model Recall is the highest, indicating that its tumor capturing ability is stronger, while its learning ability and identification efficiency are much lower than other models

poses a significant diagnostic challenge to radiologists; to address this challenge, the present study collected cranial MR images of patients with single glioblastoma and brain metastasis from a multicenter, with the It aims to establish a preoperative noninvasive discrimination model by integrating large-scale image data and advanced deep learning algorithms [26]. The introduction of a multicenter study design ensures the diversity and breadth of data sources, which can better reflect the heterogeneity of patients in different geographic regions and equipment conditions, and provides a reliable foundation for the robustness and generalizability of the model. In terms of model performance, after several rounds of rigorous training and testing, we found that the 3D ResNet-18 model demonstrated excellent performance and was able to accurately differentiate between glioblastoma and solitary brain metastases, effectively reducing the occurrence of misdiagnosis and underdiagnosis.

In the research methodology, we combined several mainstream deep learning models, including CNN as well as Transformer architecture, to explore the best diagnostic performance through model comparison and optimization. Meanwhile, a multimodal image data processing approach is also introduced in the study, which integrates image features from different sequences of conventional T1WI, T2WI, T2-FLAIR, and T1-CE in order to comprehensively capture the subtle differences in morphology, enhancement features, and microstructures of GBM and SBM. By building this deep learning-based noninvasive differentiation model, we hope to provide an efficient and reliable diagnostic tool for the differentiation of glioblastoma and brain metastases at the preoperative stage. This innovative approach not only theoretically deepens the understanding of imaging features of brain tumors, but also provides a potential auxiliary diagnostic tool for clinical practice, which is expected to be applied to actual clinical work in the future, thus improving the diagnostic and treatment process and prognostic outcomes of patients.

In the diagnosis of neurological tumors, MRI can provide high-resolution anatomical images that clearly show the complex structure of the central nervous system, including brain tissue, ventricular system, and the relationship between the lesion and the surrounding normal tissues [27]. Compared with traditional CT examination, MRI can not only locate the tumor more precisely, but also obtain more critical information about the nature of the tumor, making it the preferred examination method for patients with nervous system tumors [28]. In the diagnostic process of neurological tumors, the multimodal imaging technique of MRI is of great value. Conventional T1WI and T2WI provide the basic anatomical structure and morphological information of the tumor, which helps to initially determine the size, shape, boundary, and relationship with the surrounding tissues of the lesion [29]; whereas T1-enhanced scanning can more intuitively show the blood supply of the tumor and the destruction of the blood-brain barrier, which can provide a basis for the differentiation of malignant tumors [30]. As glioblastoma and brain metastases show similar tumor and

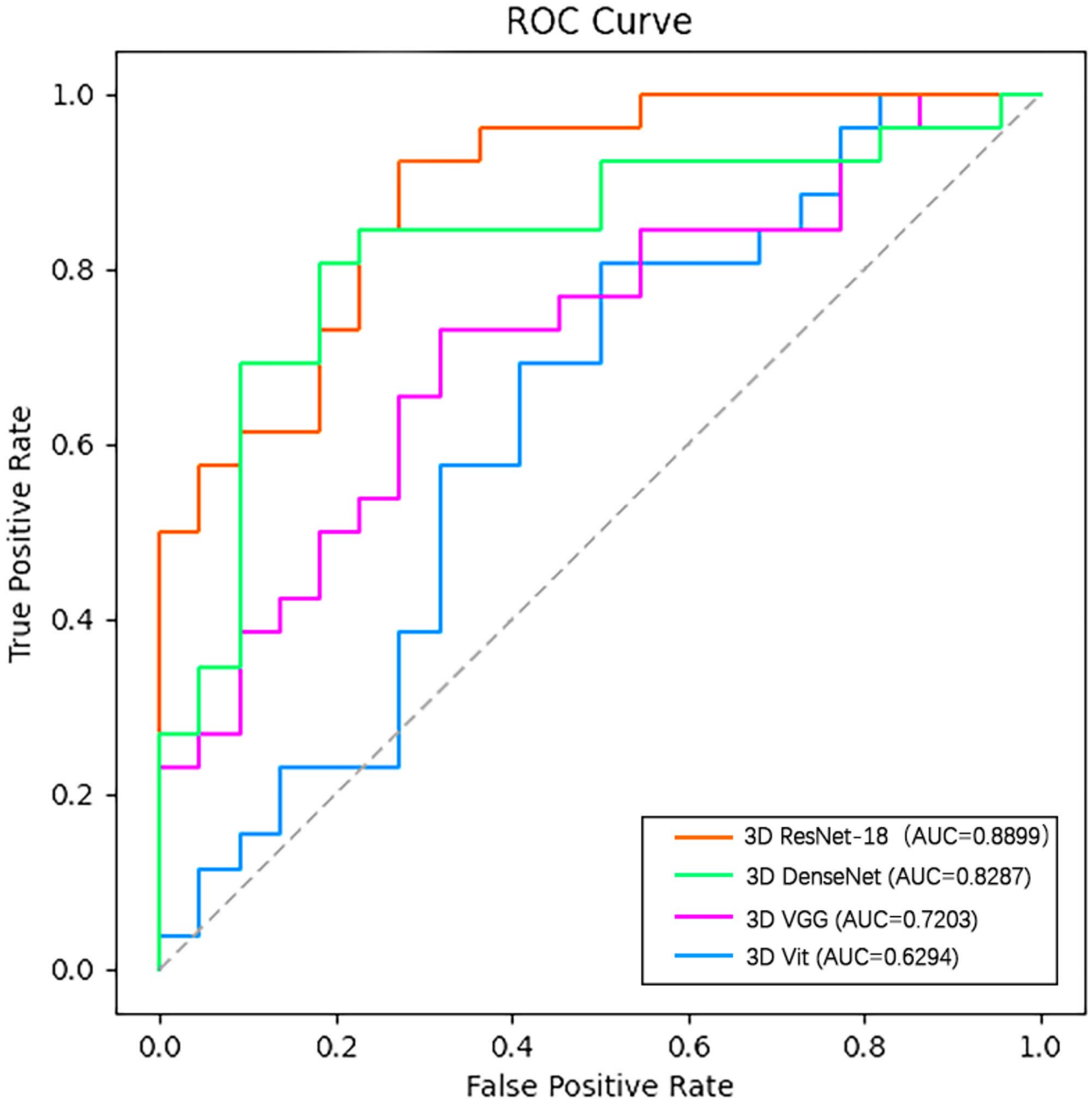


**Fig. 6** External validation ROC curves for different deep learning models

peritumor regions in MR images, several previous studies have explored the segmentation of the tumor regions of GBM and SBM [31, 32], and at the histological level, the peritumor region of GBM exhibits a high degree of heterogeneity, which is mainly composed of tumorigenic microvascular proliferation, tumor cell infiltration, and mixed mesenchymal components [33]. This complexity of the peritumor region makes GBM not only confined to the core part of the tumor, but also shows extensive invasiveness to the surrounding normal brain tissues. Therefore, on imaging presentation, the peritumoral edema of GBM is usually more diffuse and has blurred borders, reflecting the expansion path of tumor cells as well as the abnormal behavior of microscopic angiogenesis [34]. In contrast, SBM mainly exhibits vasogenic edema, which is characterized by fluid leakage from capillaries into the interstitial spaces of brain tissue, leading to the formation of localized edema [35]. However, a distinguishing feature of vasogenic edema is the lack of evidence of infiltrative tumor cells, which are histologically manifested by the relative structural integrity of the surrounding brain tissue, with no spread of tumor cells. In addition,

the peritumoral edema in SBM is usually more concentrated than in GBM, showing a well-defined border and forming a clearer demarcation from the tumor core [36]. Therefore, in our segmentation of tumors, the peritumor region was also included in the study.

As a powerful tool capable of extracting a large number of features from MR images, covering a wide range of information such as tumor morphology, texture, density, etc., imaging histology occupies an important role in the field of tumor identification. The machine learning model support vector machine (SVM) is comparable to the radiologist's discrimination ability when distinguishing GBM and MET based on MR images T2WI, apparent diffusion coefficient map (ADC), and texture parameters on T1-CE [37].Artzi et al. [38], in a study of radiohistology in combination with T1-CE images for distinguishing GBM and MET, showed that the best results were obtained using the SVM classifier model obtained the best results (AUC = 0.96) and was the best for classifying MET subtypes (breast, lung and other brain metastases). Similarly Qian [39] obtained the highest efficacy (AUC = 0.90) for distinguishing between GBM and solitary MET in a classifier using T1-enhanced images combined with support vector machine (SVM) with least absolute shrinkage and selection operator (LASSO).Su et al. [40] obtained the best results (AUC = 0.90) for distinguishing between GBM and solitary MET in a classifier using T1CE based on the minimally redundant maximal correlation (mRMR) and least absolute shrinkage and selection operator (LASSO) to establish radiomic features, with a validation cohort AUC value of 0.81. Swinburne [41] improved the diagnostic accuracy of radiologists by approximately 19% by identifying glioblastoma, brain metastases, and CNS lymphomas via a multilayer perceptron (MLP); all of these studies achieved good results, demonstrating that machine learning models can efficiently perform diagnostic analysis of GBM and brain metastatic tumors. However, these studies have certain limitations, machine learning usually takes single sequence MR images as the research object, in practice, radiologists need to judge the images through the information provided by multiple sequence MR images, and the limitations of the computational ability of machine learning in coping with multi-tasks objectively exists; moreover, it requires the researcher to spend a certain amount of time and energy in the process of feature selection and data processing.

Compared with traditional machine learning, deep learning has realized multiple improvements. In terms of model structure, deep learning has a deep neural network, and when analyzing MR images, unlike the manual extraction of features in machine learning, the deep learning model can directly extract complex tumor features from image pixels without the need to manually pre-set the extraction rules, which reduces human bias while greatly improving the efficiency and accuracy of feature extraction [42]. The relationship between the image features of a tumor and the tumor type and malignancy degree is not simple and linear, and the deep learning model is able to capture these complex nonlinear relationships, thus improving the identification accuracy [43]. In addition, deep learning performs better in multitask learning, and through techniques such as parameter sharing and joint optimization, it can effectively balance the resource allocation between different tasks, reduce the interference between tasks, and simultaneously improve the processing performance of multiple tasks, providing more comprehensive and accurate support for comprehensive tumor identification and diagnosis. In the face of massive medical image data, deep learning models can process and learn more efficiently by virtue of their powerful computational capabilities and optimization algorithms, and can still be trained and identified stably, even in the case of huge and complex data volumes. Bae et al. [44] extracted 265 radiomics features from multicenter images of T2WI and T1-CE, trained seven machine learning models with the deep learning model DNN, which showed the highest diagnostic performance in external validation (AUC = 0.956, (95% confidence interval, 0.918–0.990)), outperforming the best-performing traditional machine learning model (adaptive enhancement combined with tree-based feature selection: AUC, 0.890 (95% CI, 0.823–0.947)) and radiologist (AUC, 0.774 [95% CI, 0.685–0.852]; 0.904 [95% CI, 0.852–0.951]), which suggests that deep learning possesses better discriminative capabilities in the comparison of traditional machine learning and deep learning models.

It is worth noting that most of the previous studies did not introduce the reasons in the selection of MRI sequences, Yan et al. [45] a study, the deep learning model with multiple sequences combined had better discriminatory performance than single sequence model and the worst performance in T1WI; this is consistent with the present study, I believe that MR images with different sequences can provide different information and features, for example, T1-CE shows the destruction of the blood-brain barrier, T2-FLAIR shows peritumor edema; by learning different features, the deep learning model can better identify glioblastoma and brain metastases. T2-FLAIR shows peritumor edema; by learning different features, the deep learning model can better identify glioblastoma and brain metastases, therefore, the selection of sequences is crucial before identifying tumors by MR images. In recent years, there have been deep learning model studies on the identification of glioblastoma (GBM) and single brain metastasis (SBM) mostly using the ResNet family of network architectures

(e.g., ResNet-50, ResNet-101, ResNet-152, etc.). A deep learning model construction study based on T2WI and T1CE images showed that the ResNet-50 model outperformed radiologists in discrimination in both internal and external validation sets [46]. Although ResNet effectively solves the gradient vanishing problem in very deep network training through the residual mapping mechanism, deep network structures (e.g., more than 50 layers) still face the insufficient stability of gradient propagation and the risk of overfitting [47]. Therefore, this study makes two improvements based on the classical ResNet architecture: first, normalization is implemented on the inputs of each layer of the network to stabilize the data distribution and enhance the stability of the gradient propagation; second, an L2 regularization term is introduced into the loss function to reduce the overfitting risk by constraining the scale of the model parameters. This study innovatively adopts the 3D ResNet-18 network architecture, which is more suitable for medical imaging data characterization than the traditionally used deep networks (e.g., ResNet-50) with its streamlined 18-layer structure while maintaining the residual learning advantage. The results show that the optimized 3D ResNet-18 network exhibits significant advantages in the discriminative task of GBM vs. SBM. To explore the value of models with different architectures in two kinds of tumor identification, the deep learning models 3D VIT, 3D DenseNet and 3D VGG are introduced for the first time in this study and validated in multiple centers; in both internal and external validation, 3D ResNet-18 has the highest AUC, ACC, precision, recall, and F1 score with good robustness.

In this study, we explored the value of four deep learning models in the identification of glioblastoma and brain metastases, seeking the best identification model. We labeled the tumor body and peri-tumor region in the images of different MR sequences to provide sufficient image information for the deep learning model; Vit is a deep learning model for processing sequence data, the core of which lies in its self-attention mechanism and multi-attention mechanism, through which the model is able to efficiently deal with the complex relationships in sequence data [48],Since Vit is applied in medical images later than the CNN model, no study has been done to analyze its application in GBM and SBM discrimination. In this study, we attempted to construct a discrimination model of 3D Vit, and the AUC and accuracy in both internal and external validation sets were explicitly lower than that of the CNN model; 3D Vit performed poorly in the tumor discrimination task in this study, which may be due to the following reasons. First, 3D Vit requires a high amount of data, and the limited amount of data in this study may affect the training effect and performance of the model. Second, 3D Vit mainly relies on the global attention mechanism, which makes it relatively insensitive to local features when capturing image features. However, tumor differential diagnosis highly relies on the accurate recognition of subtle local changes, such as tumor edge morphology and texture features [49]; collectively, 3D Vit is currently immature in the field of tumor identification, and it may take a long time for research and optimization before it can be widely applied in clinical practice. The performance differences among the three CNN models, namely 3D DenseNet, 3D ResNet-18, and 3D VGG, are mainly attributed to the changes in the internal architectures of the networks, and the advantages of the ResNet network lie in its unique residual structure, which can balance the depth of the network with the stability of the training, and is suitable for complex feature extraction in medical images, while the inductive bias of the convolution is more suitable for the needs of tumor identification. DenseNet's fully-connected dense module enables feature reuse, but its parameter redundancy (about 28% increase in the number of parameters) due to the cascading of inter-layer channels may lead to slower training when the network depth is increased [50], and is prone to triggering localized feature overfitting in limited medical data scenarios.VGG mainly extracts features by stacking convolutional layers and pooling layers, and its single down sampling path leads to the difficulty of effective fusion of higher-order semantic features with lower-order texture features, and as the network deepens, it will face problems such as gradient disappearance, resulting in limited performance improvement [51]. In the identification task of GBM and SBM, 3D ResNet-18 is the preferred baseline model architecture, which can provide a reliable technical foundation for accurate identification of medical images.

Our study has several limitations. First, our data volume needs to be further expanded due to the difficulty in obtaining pathology and follow-up data for patients with single brain metastases, and smaller data samples may not provide comprehensive coverage of a variety of clinical conditions and patient characteristics, with the risk of sampling bias. Although our three-dimensional ResNet-18 model performed well in internal and external validation, its stability needs to be further tested by increasing the data volume. Second, our study did not include magnetic resonance functional imaging, such as diffusion-weighted imaging (DWI), perfusion-weighted imaging (PWI), and magnetic resonance spectroscopy (MRS), which should be included in future studies; third, our model lacked some important clinical indicators, such as immunohistochemical information, and further improvement of the model's discriminative efficacy by combining diverse clinical information will be the focus of future studies. The combination of diverse clinical

information to further improve the discriminative efficacy of the model will be the focus of future research.

## Conclusions

The combination of deep learning and magnetic resonance imaging (MRI) can efficiently identify glioblastoma and single brain metastases, and the combination of three sequences, T2WI, T1-CE, and T2-FLAIR, can provide rich and critical imaging information for the identification of the two types of tumors compared with the combination of a single sequence or other sequences. Different deep learning models have different discriminative values for glioblastoma and single brain metastases. In multicenter validation, 3D ResNet-18 has better discriminative ability than other CNN and Transformer models, shows the best robustness and generalization ability, shortens the training cycle and improves the diagnostic efficiency compared with machine learning models, and brings a new choice for clinical tumor diagnosis and treatment models.

### Abbreviations

| | |
|---|---|
| GBM | Glioblastoma |
| SBM | Solitary brain metastases |
| VIT | VisionTransformer |
| ACC | Accuracy |
| T2-FLAIR | T2- weighted fluid attenuated inversion recovery |
| T1-CE | T1-weighted contrast-enhanced imaging |
| ROC | Receiver Operating Characteristic |
| AUC | Area Under the Curve |
| ROI | Region of Interest |
| Gd-DTPA | Gadopentetic acid |
| PACS | Picture archiving and communication system |
| L2-Ridge | L2 Ridge Regression |
| ReLU | Rectified Linear Unit |
| MLP | Multilayer Perceptron |
| LASSO | Least Absolute Shrinkage and Selection Operator |

### Acknowledgements

Not applicable.

### Author contributions

Chao Kong, Ding Yan, Kai Liu and Yong Yin wrote the main manuscript text and Ma Changsheng prepared Figs. 1, 2, 3, 4 and 5. All authors reviewed the manuscript.

### Funding

This study was supported by Natural Science Foundation of China(Grant No. 82072094 and 12275162), The Scienceand Technology Foundation of Xinjiang Uygur Autonomous Region (No. 2022E02134).Shandong Medical Association Clinical Research Fund - Qilu Special Project (YXH2022ZX02197).

### Data availability

The datasets used and analyzed during the current study are available from the corresponding author on reasonable request (machangsheng_2000@126.com).

## Declarations

### Ethics approval and consent to participate

The protocol for this study was approved by the Institutional Review Committee of the Shandong Provincial Hospital and Shandong First Medical University Affiliated Cancer Hospital Ethics Committee (SDTHEC 2024001002). All experiments were conducted in strict compliance with relevant international and national guidelines and regulations regarding human research, including but not limited to ethical principles, patient rights protection, and data security requirements. As this is a retrospective study and sensitive information of all patients was hidden during the study process, so Shandong First Medical University Affiliated Cancer Hospital Ethics Committee (SDTHEC 2024001002) waived the requirement for informed consent.

### Consent for publication

Not applicable.

### Competing interests

The authors declare no competing interests.

### Author details

[1]Department of Graduate, Shandong First Medical University and Shandong Academy of Medical Sciences, Jinan, China
[2]Department of Radiation Physics, Shandong Cancer Hospital and Institute, Shandong First Medical University and Shandong Academy of Medical Sciences, Jinan, China
[3]School of Control Science and Engineering, Shandong University, Jinan, China
[4]Department of Head and Neck Comprehensive Radiotherapy, Affiliated Tumor Hospital of Xinjiang Medical University, Urumqi, China
[5]Department of Radiotherapy, Shandong Cancer Hospital and Institute, Shandong First Medical University and Shandong Academy of Medical Sciences, Jinan, Shandong Province 250117, China

Received: 23 September 2024 / Accepted: 5 May 2025
Published online: 19 May 2025

### References

1. Schaff LR, Mellinghoff IK. Glioblastoma and other primary brain malignancies in adults: A review. JAMA. 2023;329(7):574–87.
2. Gritsch S, Batchelor TT, Gonzalez Castro LN. Diagnostic, therapeutic, and prognostic implications of the 2021 world health organization classification of tumors of the central nervous system. Cancer. 2022;128:47–58.
3. Louis DN, Perry A, Wesseling P, et al. The 2021 WHO classification of tumors of the central nervous system: a summary. Neuro Oncol. 2021;23(8):1231–51.
4. Achrol AS, Rennert RC, Anders C, et al. Brain metastases. Nat Rev Dis Primers. 2019;5(1):5. Published 2019 Jan 17.
5. Sun HF, Li LD, Lao IW, et al. Single-cell RNA sequencing reveals cellular and molecular reprograming landscape of gliomas and lung cancer brain metastases. Clin Transl Med. 2022;12(11):e1101.
6. Gondi V, Bauman G, Bradfield L, et al. Radiation therapy for brain metastases: An ASTRO clinical practice guideline. Pract Radiat Oncol. 2022;12(4):265–82.
7. Moravan MJ, Fecci PE, Anders CK, et al. Current multidisciplinary management of brain metastases. Cancer. 2020;126(7):1390–406.
8. Lah TT, Novak M, Breznik B. Brain malignancies: Glioblastoma and brain metastases. Semin Cancer Biol. 2020;60:262–73.
9. Mann RM, Kuhl CK, Moy L. Contrast-enhanced MRI for breast cancer screening. J Magn Reson Imaging. 2019;50(2):377–90.
10. Zhao Y, Zhang J, Liao W, Li J, Zhang S. NUT carcinoma of the head and neck: A case report and literature review. Prec Radiat Oncol. 2024;8:138–44. https://doi.org/10.1002/pro6.1237.
11. Kamimura K, Kamimura Y, Nakano T, et al. Differentiating brain metastasis from glioblastoma by time-dependent diffusion MRI. Cancer Imaging. 2023;23(1):75. Published 2023 Aug 8.
12. Derks SHAE, van der Veldt AAM, Smits M. Brain metastases: The role of clinical imaging. Br J Radiol. 2022;95(1130):20210944.
13. Soffietti R, Ahluwalia M, Lin N, et al. Management of brain metastases according to molecular subtypes. Nat Rev Neurol. 2020;16(10):557–74.
14. Corti A, Cavalieri S, Calareso G, et al. MRI radiomics in head and neck cancer from reproducibility to combined approaches. Sci Rep. 2024;14(1):9451.
15. Okada T. Editorial for glioblastoma and solitary brain metastasis: Differentiation by integrating demographic-MRI and deep-learning radiomics signatures. J Magn Reson Imaging. 2024;60(3):921–2.
16. Lohmann P, Galldiks N, Kocher M, et al. Radiomics in neuro-oncology: Basics, workflow, and applications. Methods. 2021;188:112–21.
17. Janiesch C. Zschech P, Heinrich K. Machine learning and deep learning. Electron Markets. 2021;31(3):685–95.

18. Wang H, Jin Q, Li S, et al. A comprehensive survey on deep active learning in medical image analys is. Med Image Anal. 2024;95:103201.
19. Stahlschmidt SR, Ulfenborg B, Synnergren J. Multimodal deep learning for biomedical data fusion: A review. Brief Bioinform. 2022;23(2):bbab569.
20. Wang Y, Jian W, Yuan Z, Guan F, Carlson D. Deep learning with attention modules and residual transformations improves hepatocellular carcinoma (HCC) differentiation using multiphase CT. Prec Radiat Oncol. 2025;9:13–22.
21. Saeedi S, Rezayi S, Keshavarz H, et al. MRI-based brain tumor detection using convolutional deep learning meth ods and chosen machine learning techniques. BMC Med Inf Decis Mak. 2023;23(1):16.
22. Luo J, Pan M, Mo K, et al. Emerging role of artificial intelligence in diagnosis, classification and clinical management of glioma. Semin Cancer Biol. 2023;91:110–23.
23. Sun W, Qin Z, Deng H, et al. Vicinity vision transformer. IEEE Trans Pattern Anal Mach Intell. 2023;45(10):12635–49.
24. Li Z, Su Y, Cui Y, Yin Y, Li Z. Multi-sequence MRI-based clinical-radiomics models for the preoperative prediction of microsatellite instability-high status in endometrial cancer. Prec Radiat Oncol. 2025;9:43–53.
25. Ruff M, Kizilbash S, Buckner J. Further understanding of glioma mechanisms of pathogenesis: Implications for therapeutic development. Expert Rev Anticancer Ther. 2020;20(5):355–63.
26. Suh JH, Kotecha R, Chao ST, et al. Current approaches to the management of brain metastases. Nat Rev Clin Oncol. 2020;17(5):279–99.
27. Xu J, Zhang L, Liu Q, Zhu J. Preoperative multiparameter MRI-based prediction of Ki-67 expression in primary central nervous system lymphoma. Prec Radiat Oncol. 2025;9:23–34.
28. Mann RM, Kuhl CK, Moy L. Contrast-enhanced MRI for breast cancer screening. J Magn Reson Imaging. 2019;50(2):377–90.
29. Derks S. Brain metastases: The role of clinical imaging. Br J Radiol. 2022;95(1130):20210944.
30. Roesler R, Dini SA, Isolan GR. Neuroinflammation and immunoregulation in glioblastoma and brain metas tases: Recent developments in imaging approaches. Clin Exp Immunol. 2021;206(3):314–24.
31. Ahsan R, Shahzadi I, Najeeb F, Omer H. Brain tumor detection and segmentation using deep learning. MAGMA. 2025;38(1):13–22.
32. Zarenia E, Far AA, Rezaee K. Automated multi-class MRI brain tumor classification and segmentation using deformable attention and saliency mapping. Sci Rep. 2025;15(1):8114.
33. Venkataramani V, Yang Y, Schubert MC, et al. Glioblastoma hijacks neuronal mechanisms for brain invasion. Cell. 2022;185(16):2899–917.e31.
34. He L, Zhang H, LI T, et al. Distinguishing tumor cell infiltration and vasogenic edema in the Peri tumoral region of glioblastoma at the voxel level via conventional MRI sequences. Acad Radiol. 2024;31(3):1082–90.
35. Heynold E, Zimmermann M, Hore N, et al. Physiological MRI biomarkers in the differentiation between Glioblastomas and solitary brain metastases. Mol Imaging Biol. 2021;23(5):787–95.
36. Parvaze PS, Bhattacharjee R, Verma YK, et al. Quantification of radiomics features of peritumoral vasogenic edema extracted from fluid-attenuated inversion recovery images in glioblastom a and isolated brain metastasis, using T1-dynamic contrast-enhanced pe Rfusion analysis. NMR Biomed. 2023;36(5):e4884.
37. Priya S, Liu Y, Ward C, et al. Machine learning based differentiation of glioblastoma from brain meta stasis using MRI derived radiomics. Sci Rep. 2021;11(1):10478.
38. Artzi M, Bressler I, Ben Bashat D. Differentiation between glioblastoma, brain metastasis and subtypes using radiomics analysis. J Magn Reson Imaging. 2019;50(2):519–28.
39. Qian Z, Li Y, Wang Y, Et. Differentiation of glioblastoma from solitary brain metastases using radiomic machine-learning classifiers. Cancer Lett. 2019;451:128–35.
40. Su CQ, Chen XT, Duan SF, et al. A radiomics-based model to differentiate glioblastoma from solitary brain metastases. Clin Radiol. 2021;76(8):629.e11-.e18.
41. Swinburne NC, Schefflein J, Sakai Y, et al. Machine learning for semi-automated classification of glioblastoma, brain metastasis and central nervous system lymphoma using magnetic resonance advanced imaging. Ann Transl Med. 2019;7(11):232.
42. Erickson BJ. Basic artificial intelligence techniques: Machine learning and deep learning. Radiol Clin North Am. 2021;59(6):933–40.
43. Jiang Y, Yang M, Wang S, et al. Emerging role of deep learning-based artificial intelligence in tumor pathology. Cancer Commun (Lond). 2020;40(4):154–66.
44. Bae S, An C, Ahn SS, et al. Robust performance of deep learning for distinguishing glioblastoma from single brain metastasis using radiomic features: Model development and validation. Sci Rep. 2020;10(1):12110.
45. Yan Q, Li F, Cui Y, et al. Discrimination between glioblastoma and solitary brain metastasis using conventional MRI and diffusion-weighted imaging based on a deep learning algorithm. J Digit Imaging. 2023;36(4):1480–8.
46. Shin I, Kim H, Ahn SS, et al. Development and validation of a deep Learning-Based model to distinguish glioblastoma from solitary brain metastasis using conventional MRI mages. AJNR Am J Neuroradiol. 2021;42(5):838–44.
47. Xu W, Fu Y-L, Zhu D. ResNet and its application to medical image processing: Research progress and challenges. Comput Methods Programs Biomed. 2023;240:107660.
48. Han K, Wang Y, Chen H, et al. A survey on vision transformer. IEEE Trans Pattern Anal Mach Intell. 2023;45(1):87–110.
49. Elbedwehy S, Medhat T, Hamza T, et al. Efficient image captioning based on vision transformer models. CMC-Comput Mat Contin. 2022;73(1):1483–500.
50. Zhou T, Ye X, Lu H, et al. Dense convolutional network and its application in medical image analysis. Biomed Res Int. 2022:2384830.
51. Zeng S, Chen H, Jing R, et al. An assessment of breast cancer HER2, ER, and PR expressions based on mammography using deep learning with convolutional neural networks. Sci Rep. 2025;15(1):4826.


## Publisher's note